

# Dynamically tuned design of the MFI thorax \*

S. Avadhanula, R. J. Wood, D. Campolo, R. S. Fearing  
{srinath, rjwood, minmo, ronf}@eecs.berkeley.edu  
Department of EECS, University of California, Berkeley, CA 94720

## Abstract

*This paper presents an analysis of the major mechanical component (the thorax) of the micromechanical flying insect (MFI), a centimeter sized aerial vehicle currently in development at UC Berkeley. We present a description of the kinematics of the mechanism which converts piezoelectric actuation into complex 3D wing motion. A complete non-linear modeling of the system based on the Lagrangian energy technique is presented. A design methodology is presented in order to achieve optimal matching conditions. Two kinds of sensors which are presently utilized on the MFI are described. Experimental results are presented which validate some of the modeled non-linear aspects of the mechanism.*

## 1 Introduction

Micro-aerial flying mechanisms are an attractive form of locomotion because of their many potential applications such as search and rescue, exploration, sensor distribution, reconnaissance, etc. made possible by their very small size and high maneuverability. Early work on microrobotic flight was done by Shimoyama *et al* [11], while different aspects and approaches to micro areal flight have been pursued by various groups ([3]-[8]). Fundamental work by Dickinson *et al* [4] showed that the complex high speed motion of the insect wings is responsible for creating unsteady aerodynamic effects which account for the exceptional lift and agility exhibited by insects. A *biomimetic* approach was subsequently undertaken by Fearing *et al* [5] to design a wing transmission which had the same degrees of freedom as the actual insect. Early designs for the mechanism involved a fan-fold wing technique. Recently, the design was modified to enable the use of rigid wings to achieve the same motion [14]. This technique avoids some of the aerodynamic and fabrication problems involved with the original design. Initial attempts at modeling the dynamics of the differential [14] assumed a lumped model

\*This work was funded by ONR MURI N00014-98-1-0671, DARPA and NSF KDI ECS 9873474.

approach in which the wing motion was separated into rotations about uncoupled axes.

This paper describes a detailed dynamic model of the thorax, a design methodology for the optimal design of the thorax and the sensors which are currently utilized on the MFI.

## 2 Mechanism Description

The MFI utilizes piezoelectric actuators which deflect under the action of an applied electric field [12]. The overall transmission from the actuators to the wing can be broken up into 2 distinct parts. The first stage consists of a planar fourbar which converts small translational input from the piezo into large angular motion at the output. (typically about  $60^\circ$  for 3 mm).

The next stage of the mechanism consists of the wing differential mechanism which converts 2 independent angular inputs into a coupled *flapping* and *rotation* of the wing.

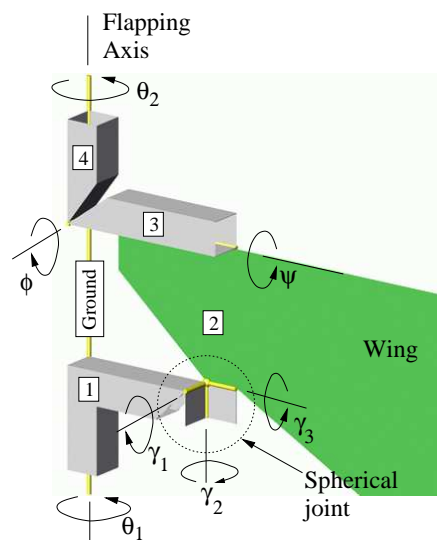


Figure 1: Kinematic representation of the wing differential mechanism.

The wing differential is essentially a spatial five-bar mechanism (with topology RSRRR) with 2 degrees of freedom. It can be considered a variation of the spherical fourbar mechanism described in [9], where one of

the intersecting revolute joints is replaced by a spherical joint. The various links are labeled in Fig. 1. The fourbars drive the links 1 and 4 directly. The wing itself forms link 2 of the mechanism (in practice, link 2 is made of a steel beam with the wing glued onto it.) When the fourbars move in phase, then the whole differential simply rotates about the global flapping axis. This is defined as pure flapping. When the 2 fourbars move out of phase, i.e  $\theta_1 \neq \theta_2$ , then the wing also rotates about link 2 through an angle  $\psi$  defined as rotation in addition to some flapping. This is described precisely in the next section.

### Notation

$\theta_1, \theta_2$	Fourbar actuations
$\alpha$	( := $\theta_1 - \theta_2$ ) phase difference between the 2 spars
$\phi$	Deviation of wing from stroke plane
$\psi$	Rotation angle of the wing

## 3 Kinematics

In this section, we derive the forward and inverse kinematics of the wing differential mechanism. It can be shown that the wing rotation  $\psi$ , and the stroke plane deviation  $\phi$ , depend on the phase difference  $\alpha$  as

$$\psi = \sin^{-1}(\lambda \sin \alpha) \quad (1)$$

$$\phi = \sin^{-1} \left( \frac{1}{\sqrt{\lambda^2 + \cos^2 \psi}} \right) - \tan^{-1} \left( \frac{\cos \psi}{\lambda} \right), \quad (2)$$

where

$$\lambda := \frac{l}{d} \quad (3)$$

In the following discussion, the ratio  $l/d$ , denoted by  $\lambda$ , is referred to as the differential transmission ratio. It is evident from eqn 1 that a larger transmission ratio means that for a constant phase difference  $\alpha$ , we obtain a larger rotation  $\psi$ . We are interested in transmission ratios with values  $\geq 1$ , due to factors such as dynamic balancing (which is explained later) and also getting the desired kinematic trajectories from the wing. Fig.2(a) shows the variation of  $\psi$  with  $\alpha$  for  $\lambda$  between 1 and 2.5. We see that the phase difference required to generate the same rotation decreases with increasing  $\lambda$ . Furthermore, the amount of non-linearity in the transmission also increases with  $\lambda$ .

### 3.1 Inverse kinematics of the Spherical Joint

As shown in Fig. 1, the spherical joint consists of 3 flexures in parallel in order to achieve independent

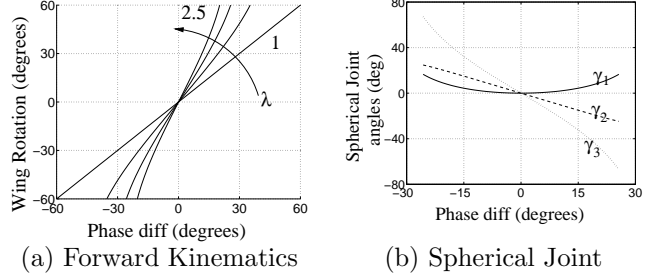


Figure 2: Kinematics of the Wing Differential.

rotations about 3 axes. In order to find out the equivalent stiffness of the wing differential we will need to find out the angles through which each of these flexures rotate for a given angle of attack. Fig. 2(b) shows the variation of the joints in the spherical joint with phase difference for  $\lambda = 2$ . It shows that  $\gamma_3$  joint contributes quite a lot more to the overall stiffness of the spherical joint than the  $\gamma_1$  and  $\gamma_2$  joints.

## 4 Dynamics

We use the Euler-Lagrange formalization to derive the dynamics of the system. In order to do this, the various energy terms in the mechanism have to be calculated in terms of the state variables.

$$KE = KE_{\text{actuators}} + KE_{\text{four-bars}} + KE_{\text{spars}} + KE_{\text{wing}} \quad (4)$$

$$PE = PE_{\text{actuators}} + PE_{\text{differential}} \quad (5)$$

The kinematics described in section 3 enable the formulation of the various terms above in terms of  $\theta_2, \alpha, \dot{\theta}_2$  and  $\dot{\alpha}$ . Therefore defining  $\{\theta_2, \alpha\}^T$ , as the state variables and transforming variables, we get the following differential equation of motion (details of the derivation can be found in [1]):

$$\mathbf{M} \begin{bmatrix} \ddot{\theta}_1 \\ \ddot{\theta}_2 \end{bmatrix} + \mathbf{b} \begin{bmatrix} \dot{\theta}_1 \\ \dot{\theta}_2 \end{bmatrix} + \mathbf{K} \begin{bmatrix} \theta_1 \\ \theta_2 \end{bmatrix} + \begin{bmatrix} \frac{1}{2} m'_{w,2} (\dot{\alpha})^2 \\ -\frac{1}{2} m'_{w,2} (\dot{\alpha})^2 \end{bmatrix} = \begin{bmatrix} \tau_1 \\ \tau_2 \end{bmatrix} \quad (6)$$

where

• Mass  $\mathbf{M} =$

$$\begin{bmatrix} \left( \begin{array}{c} m_{s,1} + m_{w,2} \\ + m_{fb,1} + m_{act,1} \end{array} \right) & m_{w,12} - m_{w,2} \\ m_{w,12} - m_{w,2} & \left( \begin{array}{c} m_{s,2} + m_{fb,2} \\ + m_{act,2} + m_{w,2} \\ + m_{w,1} - 2m_{w,12} \end{array} \right) \end{bmatrix} \quad (7)$$

The main contribution to the inertia matrix comes from the wing and appears as  $m_{w,1}$ ,  $m_{w,2}$  and  $m_{w,12}$  which are the inertia components of the wing lamina reflected through the differential transmission. These depend non-linearly on both the differential transmission ratio,  $\lambda$  and the phase difference,  $\alpha$ .

$$\begin{bmatrix} m_{w,1} \\ m_{w,2} \\ m_{w,12} \end{bmatrix} = \begin{bmatrix} c_\phi^2 & 1 - c_\psi^2 \cdot c_\phi^2 \\ \phi'^2 & \phi'^2 c_\psi^2 + \psi'^2 \\ 0 & \phi' s_\psi c_\phi - \psi' s_\phi \end{bmatrix} \begin{bmatrix} -s_{2\phi} c_\psi \\ -2\phi' \psi' s_\psi \\ \psi' c_\phi c_\psi + \phi' s_\phi s_\psi \end{bmatrix} \begin{bmatrix} J_{xx} \\ J_{zz} \\ J_{xz} \end{bmatrix}, \quad (8)$$

where the dependence of  $\phi$  and  $\psi$  on  $\lambda$  and  $\alpha$  are given in equations 1-2 and  $J_{xx}, J_{zz}, J_{xz}$  are the fixed inertia components of the wing. The equation above simplifies considerably about the nominal position of the differential i.e for  $\alpha = 0$ . For  $\alpha = 0$ , we have:

$$\begin{bmatrix} m_{w,1} \\ m_{w,2} \\ m_{w,12} \end{bmatrix} = \begin{bmatrix} 1 & 0 & 0 \\ 0 & \lambda^2 & 0 \\ 0 & 0 & \lambda \end{bmatrix} \begin{bmatrix} J_{xx} \\ J_{zz} \\ J_{xz} \end{bmatrix} \quad (9)$$

The terms  $m_{s,1/2}$  in eqn. 7 are the inertias of links 1 and 4 of the differential. Currently, these spars are made out of 12.5 micron thick stainless steel folded into square and triangular beams 1 mm on each side using the methods described in [10]. For the current design, the length of the spars (i.e links 1 and 3 in Fig. 1) is fixed at 2 mm and the differential transmission ratio is varied by changing the spacing between them. Consequently, the spar inertias are fixed at  $2 \times 10^{-12}$  and  $3 \times 10^{-12}$   $kg \cdot m^2$  respectively.

Also, the terms  $m_{fb,1/2}$  in eqn. 7 are the inertias of the two fourbars which transmit motion from the PZTs to the wing differential. Their design is also fixed (details in [1]) and consequently, their inertias are fixed at approximately  $1.7 \times 10^{-12} kg \cdot m^2$  each.

Finally the terms  $m_{act,i}$  in eqn. 7 is the equivalent rotational inertia of the PZT reflected about the wing hinge. Assuming a linear fourbar transmission, we have

$$m_{act,i} = m_{PZT,i} / N_f^2, \quad i = 1, 2 \quad (10)$$

where  $N_f$  is the fourbar transmission and  $m_{PZT,1/2}$  is the linear inertia of the PZT measured at the point of actuation.

- **Damping** The aerodynamic forces felt by an insect wing during its motion are quite non-linear

and time-varying [4]. However, for the sake of analysis, we use a linear damping matrix to approximate them. It should be noted that the linear damping term is calculated so that it overestimates the drag force felt on the wing at every instant except when it achieves the peak velocity [14].

$$\mathbf{b} = \begin{bmatrix} b_2 & b_{12} - b_2 \\ b_{12} - b_2 & b_2 + b_1 - 2b_{12} \end{bmatrix} \quad (11)$$

The most dominant term of the damping matrix is  $b_1$  and determines the  $Q$  of the wing in a simple flapping mode. Preliminary measurements of the structural  $b$  yielded an estimate of  $7 \times 10^{-9} Nms/rad$ .

- **Stiffness** The stiffness matrix of the thorax mechanism is given by

$$\mathbf{K} = \begin{bmatrix} k_{s,1} + k_d & -k_d \\ -k_d & k_{s,2} + k_d \end{bmatrix} \quad (12)$$

where,  $k_d$ , called the differential stiffness is defined as

$$k_d := \frac{1}{\alpha} \frac{\partial PE_{\text{differential}}}{\partial \alpha} \quad (13)$$

The differential stiffness arises from the flexures which make up the joints of the mechanism. Each flexure can be considered a simple rotational spring whose stiffness depends on the dimensions of the flexure such as length, thickness and width and also the material of the flexure (see [7] for a complete treatment of flexures). We presently use 6.3 micron thick polyester flexures ( $E = 2.5 GPa$ ). Changing the flexure lengths provides the ability to change the differential stiffness for a given transmission ratio. Fig. 3 shows the variation of  $k_d$  with  $\lambda$  and  $\alpha$  for a typical wing differential where the major flexures are made of 6.3 micron thick polyester flexures 175 microns long and 1 mm wide. We see that  $k_d$  increases with the  $\lambda$

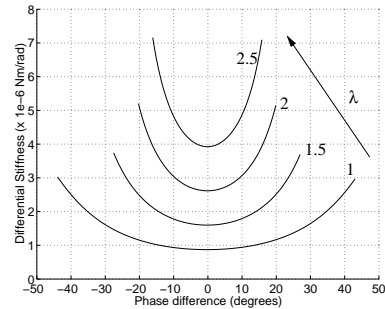


Figure 3: Variation of differential stiffness with  $\lambda$  and  $\alpha$ .

as is to be expected. Also, the non-linearity in  $k_d$  increases sharply with  $\lambda$ . (A linear differential would have had a constant stiffness for all  $\alpha$ .)  $k_{s,1}$  and  $k_{s,2}$  in equation 12 represent the actuator stiffness reflected about the wing hinge.

$$k_{s,i} = \frac{k_{act,i}}{N_f^2}, \quad i = 1, 2 \quad (14)$$

where  $N_f$  is the fourbar transmission ratio and  $k_{act,i}$  is the linear stiffness of the actuator measured at the point of actuation.

## 5 Design Synthesis

Once the differential equations are set up, we want to design the differential mechanism to get good behavior from the mechanism. As a first step, we set up a metric for evaluating the performance of a differential equation. We then try to design a mechanism which will satisfy this differential equation.

### 5.1 Performance Metric

Consider the linearized frequency response of (6) for some typical values of  $k_d$ ,  $J_{xx}$ ,  $J_{xz}$ , etc shown in Fig. 4.  $A_{11}$  represents the amplitude of motion of spar 1 (link 1 in Fig. 1) when only the first actuator is driven with the resonance at  $f_1$ . Similarly  $A_{22}$  represents the amplitude of motion of spar 2 (link 4 in Fig. 1) with actuator 2 driven.  $A_{12}$  represents the *cross-coupling*. It represents the motion of spar 2 when actuator 1 is driven. A large  $A_{12}$  means that the actuators begin to interfere with each other, making it harder to drive them out of phase. The frequency response, while not

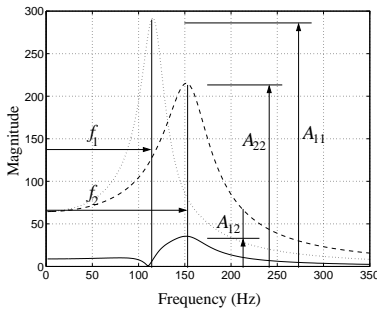


Figure 4: Performance of a typical 2 input 2 output  $2^{nd}$  order system.

what we desire serves to illustrate some of the characteristics we design for:

1. **Symmetry** The transfer functions from  $\tau_1$  to  $\theta_1$  should have the same resonant frequency as the transfer function from  $\tau_2$  to  $\theta_2$ , i.e  $f_1 = f_2$ . This will ensure that we can drive the two spars in

resonance at the same frequency. This condition implies the following condition on the system parameters:

$$\frac{k_{s,1} + k_d}{m_{s,1} + m_2} = \frac{k_{s,2} + k_d}{m_{s,2} + m_2 + m_1 - 2m_{12}} \quad (15)$$

Furthermore, the amplitude of motion at resonance should be about the same for both spars, i.e  $A_{11} = A_{22}$ , which gives the condition that:

$$b_2 = b_2 + b_1 - 2b_{12} \quad (16)$$

2. **Small cross-coupling** It's desirable to be able to drive the two spars independently. This will ensure that we are able to generate sufficient phase differences and correspondingly sufficient angles of attack. For small cross-coupling at DC, the off-diagonal terms in (12) should be small which implies:

$$k_d \ll k_{s,1}, k_{s,2} \quad (17)$$

For small cross-coupling at AC, the off-diagonal terms in the mass and damping matrices should be small, which implies:

$$m_{12} - m_2 \approx 0 \quad (18)$$

$$b_{12} - b_2 \approx 0 \quad (19)$$

These *matching conditions*, (15-19) can be expanded to:

$$\begin{aligned} k_d &\ll k_{s,1} & m_{w,1} &= 2m_{w,2} \\ k_{s,1} &= k_{s,2} & b_1 &= 2b_{12} \\ m_{s,1} &= m_{s,2} & b_2 &= b_{12} \\ m_{w,1} &= 2m_{w,12} \end{aligned} \quad (20)$$

The design effort now involves choosing the various parameters of the mechanism in order to approach the matching conditions given above. The parameters in the construction of the wing mechanism are:

1. **Fourbar Transmission Ratio,  $N_f$ :** The fourbar transmission ratio effects the reflected stiffness of the actuator (10) and also the DC response of the mechanism. The resonant frequency decreases linearly with the transmission ratio while the DC motion increases linearly with the transmission ratio.
2. **Differential Transmission Ratio,  $\lambda$ :**  $\lambda$  affects how the constant wing inertia terms  $[J_{xx}, J_{xz}, J_{zz}]'$  are mapped to the wing hinge (8). The differential transmission ratio also effects the reflected stiffness of the differential mechanism. (Fig. 3).

- Flexure Design:** The flexures in the wing differential have to be designed for a low parallel stiffness while avoiding resonant modes due to serial compliance in undesirable directions, which might occur if the flexures are made too long.
- Wing Shape:** The wing shape is not a single parameter. It includes information about how the mass is distributed over the wing area. In our case the shape can be completely specified by the three inertia parameters,  $J_{xx}$ ,  $J_{zz}$  and  $J_{xz}$ .

## 5.2 Fabrication

Fig. 5(a) shows the wing differential fabricated to final scale. The top spar can be seen to be slightly leading the bottom spar causing a positive angle of attack. The fabrication, while retaining the kinematics previously defined, is significantly different than the schematic (Fig. 1) due to considerations of flexure width optimization, and ease of assembly and alignment.

The main difficulties were encountered in the fabrication process were firstly, that the flexures currently employed in the MFI are made of 6.3 micron polyester. It was found that the lowest differential stiffness achieved with this material is still more than 50% of the actuator stiffness. This is not quite low enough to get the desired uncoupling. Secondly, the PZT actuator used on the structure turned out to have a stiffness of 113  $N/m$ . This was about 50% less than the anticipated actuator stiffness. In future versions, a lower fourbar transmission ratio will be used to counter this effect. The lower stiffness resulted in a decreased resonance and increased coupling at resonance.

These factors lead to a differential which exhibited more coupling than is optimal. From the point of view of validating the model, however, the present thorax is better since a differential with more coupling exhibits rather more “interesting” behavior than a totally uncoupled differential and is much harder to predict. Section 6 describes some of the experiments which were undertaken to test the validity of the model.

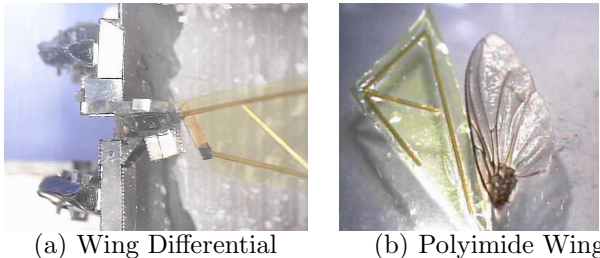


Figure 5: Photo of MFI wing differential mechanism.

Fig. 5(b) shows the wing used in the current MFI. This wing consists of a face sheet made of 7 micron thick polyimide with 200 micron diameter  $\times$  10 micron thick polyimide tubes laid across it. (See [1] for fabrication details). The primary purpose of the tubes is to provide the necessary stiffness to the wing while also enhancing the inertial properties of the differential. Table 1 is a brief comparison of the current wing with a calliphora wing (since the calliphora weighs nearly as much as the target MFI.) The main advantages of this wing were the ease of fabrication and more importantly the highly repeatable and accurate manner in which the required low inertia could be obtained.

	MFI wing	Calliphora wing
Weight	0.48 $mg$	1.0 $mg$
Moment of Inertia	21 $mg \cdot mm^2$	22 $mg \cdot mm^2$
Moment of Area (Flapping)	1100 $mm^4$	900 $mm^4$

Table 1: Comparison of the MFI wing with a Calliphora wing.

## 6 Experimental Results

Linearizing (6) about an operating point yields a transfer function matrix which relates the two input torques  $\tau_1$  and  $\tau_2$  to the two spar angles  $\theta_1$  and  $\theta_2$ .

$$\begin{bmatrix} \theta_1 \\ \theta_2 \end{bmatrix} = \underbrace{\begin{bmatrix} G_{11}(s) & G_{12}(s) \\ G_{21}(s) & G_{22}(s) \end{bmatrix}}_{=: G(s)} \begin{bmatrix} \tau_1 \\ \tau_2 \end{bmatrix} \quad (21)$$

The effect of non-linearity in the model is to change the transfer function above for different operating points.

The experimental results presented here involved measurement of the frequency response of the system for small amplitudes about two different operating points.

- $\alpha = \theta_1 - \theta_2 = 0^\circ$ . The differential stiffness is at a minimum when the two spars are in phase and we expect the most uncoupling in this situation. Fig. 6(a) shows the predicted frequency response for this operating point.
- $\alpha = \theta_1 - \theta_2 = 25^\circ$ . At this phase difference, the differential stiffness is almost 3 times its nominal value. Fig. 6(b) shows the predicted frequency response for this operating point. The major difference between the two is that the second resonance moves from 150 Hz to more than 220 Hz.

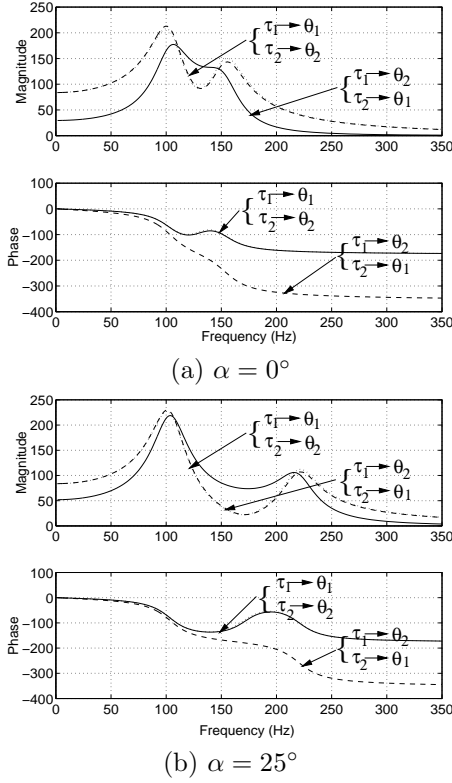


Figure 6: Predicted frequency response of the wing differential.

## 6.1 Strain Gage Sensing / Results

The deflection of the PZT actuators depends on both the applied electric field and the reaction force on the actuator from the fourbar [16],[17]. This fact can be used to fashion a state estimator which measures the torques acting on the spars ( $\tau_1$ ,  $\tau_2$ ) as well as the wing angles ( $\theta_1$  and  $\theta_2$ ). The state estimator uses the applied electric field applied to the actuators as the input and the moments at the base of the actuator as outputs. These moments are measured using 1 DOF semiconductor straingages [2],[15].

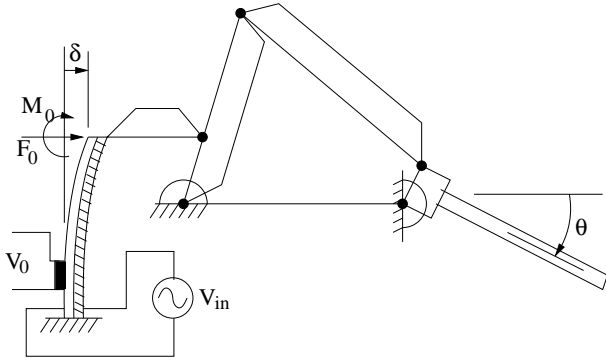


Figure 7: Strain gage sensing.

The signal generated by the strain gages,  $V_0$  and the tip displacement of the actuator,  $\delta$  is given by:

$$\begin{aligned} \delta &= C_1 V_{in} + C_2 F_r \\ V_0 &= C_3 V_{in} + C_4 F_r, \end{aligned} \quad (22)$$

where the parameters  $C_1, C_2, C_3$  and  $C_4$  are  $2 \times 2$  matrices which contain the material and physical properties of the actuator and strain sensor. We can readily measure the frequency response of the strain gage dynamics ( $V_0/V_{in}(s)$ ) using a dynamic signal analyzer (DSA), HP3562A. We are primarily interested in relating the thorax dynamics  $G(s)$  to the above measurement. It can be shown that the measurement dynamics and the structural dynamics are related as (details in [13]):

$$\frac{V_0}{V_{in}}(s) = C_3 + C_4(G(s) - m_{act}s^2) \times (I_2 - C_2(G(s) - m_{act}s^2))^{-1} C_1 \quad (23)$$

In practice, a state space approach is used to relate the measurement and thorax dynamics. This avoids numerically unsound calculations such as inversion of transfer function matrices. Figs. 8(a) and 8(b) show the comparison of the actual and predicted strain gage signals. Fig. 8(a) corresponds to the case when the sensing actuator is the same as the drive actuator. Fig. 8(b) represents the cross-coupling, i.e when we sense the motion of the non-driven actuator. Both these measurements were taken for  $\alpha = \psi = 0^\circ$  and show the double peak characteristic of the coupling between the two sides of the structure.

## 6.2 Electrical Sensing

Piezo-electric actuators link their mechanical and electrical domains in a bi-directional fashion[6]. This property enables the use of the piezo-electric actuators as sensors. Fig. 9 shows a representation of the actuator as a two-port element, where  $C_0$  and  $R_0$  represent the electrical capacitance and resistance (losses) of the actuator (and can be measured before-hand) and  $C_m$  represents the mechanical compliance of the actuator ( $C_m = 1/k_{act}$ ).  $T_p$  represents the transmission ratio of the actuator from the electrical to the mechanical domain.

The total admittance of the actuator as seen from the electrical domain can be calculated as

$$\begin{aligned} Y &= Y_0(\omega) + Y_1(\omega) \\ &= Y_0(\omega) + T_p^2 Y_m(\omega) \\ &= \frac{j\omega C_0}{1 + j\omega R_0 C_0} + T_p^2 Y_m(\omega) \end{aligned} \quad (24)$$

We are primarily interested in extracting the mechanical admittance of the structure  $Y_m(\omega)$ . To do this, we

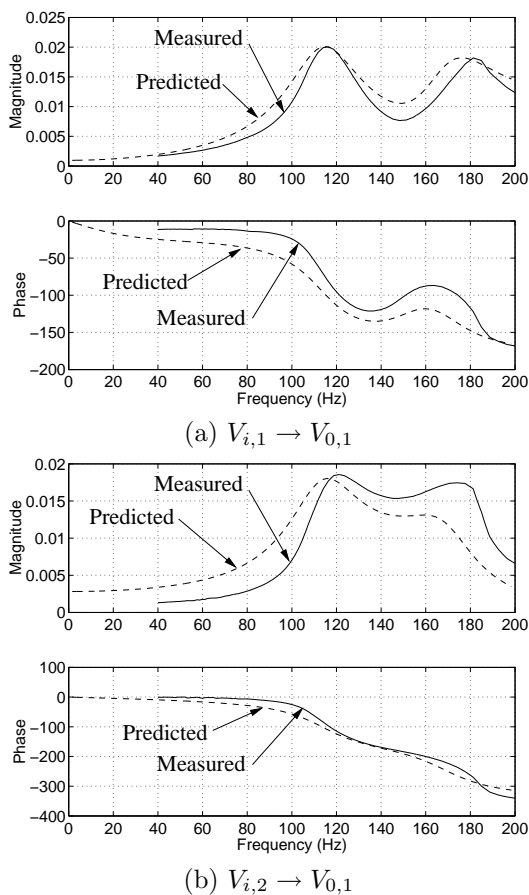


Figure 8: Comparison of predicted (dashed) and actual (solid) strain gage dynamics. (a)  $\alpha = 0^\circ$  (b)  $\alpha = 25^\circ$ .

proceed by measuring  $Y(\omega)$ , which can be calculated as:

$$Y(\omega) = j\omega C_s \left( \frac{V_0/V_{in}}{1 - V_0/V_{in}} \right) \quad (25)$$

$V_0/V_{in}$  is readily measured using a DSA. Subtracting the effect of  $C_0, R_0$  using eqn. 24 yields the required mechanical admittance of the structure  $Y_m(\omega)$ .

Figs. 10(a) and 10(b) show a comparison of the measured mechanical admittance  $Y_m(\omega)$  and with the frequency response predicted by the model for the cases where  $\alpha = 0^\circ$  and  $\alpha = 25^\circ$ . A single scaling factor was used to match the maximum amplitudes of the measurement and the simulation. This scaling takes into account the transmission ratios such as  $T_p$ , the electromechanical transmission ratio of the PZT and  $N_f$ , the amplification ratio of the fourbar. We see a validation of an important effect of the system non-linearity, where a change in the set-point changes the frequency response of the system radically. Fig. 10(a) shows a double resonance while Fig. 10(b) shows a sin-

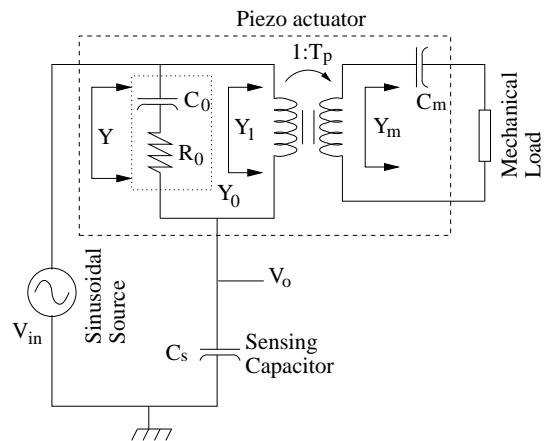


Figure 9: Using the piezo-electric actuator as a mechanical admittance sensor.

gle resonance (before 200 Hz) which is characteristic of high coupling.

## 7 Conclusions

A full non-linear modeling of dynamics of the thorax, the major mechanical component of the MFI is presented. A strategy for choosing the various fabrication parameters is presented in order to optimize the expected performance of the system. Two kinds of sensors which are presently used on the MFI are discussed. The non-linear aspects of the system are validated by observing the frequency response of the system and its variation with changing operating points.

Inspite of several constraints in the present fabrication setup which were mentioned earlier, we observed satisfactory wing trajectories from the thorax. In particular, we achieved inertial matching so that both actuators had the same loaded resonant frequencies, enabling them to be operated simultaneously with equal effectiveness.

We are presently investigating other materials for making flexures such as HS-2 (silicone-rubber), which has a low elastic modulus and has potential for making very low parallel stiffness flexures. Problems such as clamping, adhesion will have to be overcome for successful implementation. Future work will also involve system identification on the structure to fine-tune the values of various model parameters using the techniques presented in section 6. Control strategies will be employed to assess the extent of uncoupling required to generate the required wing trajectories.

## Acknowledgments

The authors would like to thank Joseph Yan for valuable discussions on structural kinematics, Gabe

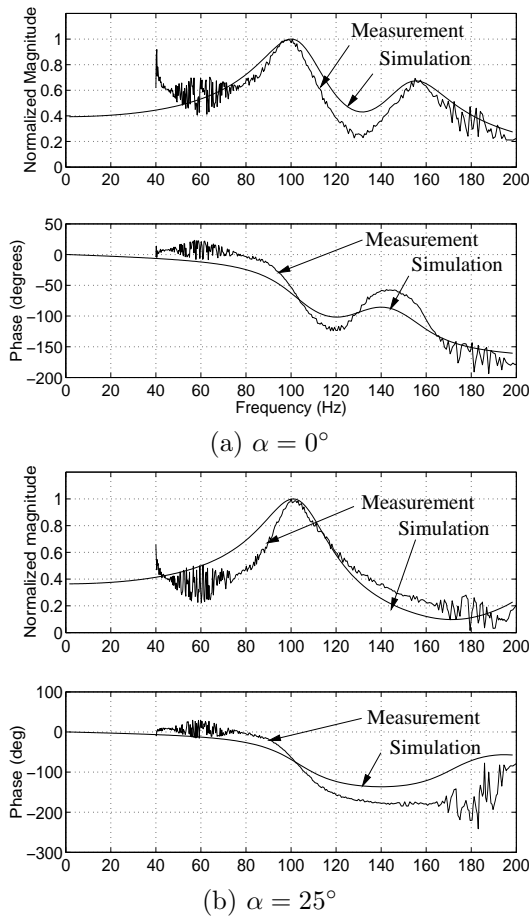


Figure 10: Comparison of experimental and simulated frequency responses using piezo-electrical sensing.

Moy for numerous suggestions on design and fabrication issues and Metin Sitti and Eric Park for helping with the fabrication and modeling of the PZT actuators.

## References

- [1] S. Avadhanula, "The design and fabrication of a dynamically tuned MFI thorax," MS Thesis, University of California, Dec 2001.
- [2] A. Bicchi, A. Caiti, and D. Prattichizzo, "Optimal design of a multi-axis force/torque sensor," *38<sup>th</sup> Conf. on Decision and Control*, pages 2981–2986, Phoenix, USA December 1999.
- [3] A. Cox, E. Garcia, and M. Goldfarb, "Actuator development for a flapping microrobotic MAV," In *SPIE Microrobotics Symp.*, pages 102–108, Boston, MA, Nov 1998.
- [4] M.H. Dickinson, F-O. Lehmann, and S.P. Sane, "Wing rotation and the aerodynamic basis of insect flight," *Science*, 284:1954–1960, June 1999.
- [5] R.S. Fearing, K.H. Chiang, M.H. Dickinson, D.L. Pick, M. Sitti, and J. Yan, "Wing transmission for

- a micromechanical flying insect," *IEEE Int. Conf. on Robotics and Automation*, pages 1509–1516, San Francisco, CA, April 2000.
- [6] M. Goldfarb and N. Celanovic, "Modelling Piezoelectric Stack Actuator for Control of Micromanipulation," *IEEE Control Sys. Magazine*, vol. 17, no. 3, pp. 69–79, 1997.
- [7] M. Goldfarb, J.E. Speich, "A Well-behaved revolute flexure joint for compliant mechanism design," *Transactions of the ASME*, Vol 121, pages 424–429, September 1999.
- [8] T.N. Pornsin-Sirirak, S.W. Lee, H. Nassef, J. Grasmeyer, Y.C. Tai, C.M. Ho, and M. Keennon, "MEMS wing technology for a battery-powered ornithopter," In *IEEE 13th Annual Int. Conf. on MEMS*, pages 799–804, Piscataway, NJ, Jan 2000.
- [9] D. A. Ruth and J. M. McCarthy, "The Design of Spherical 4R Linkages for Four Specified Orientations," *Computational Methods in Mechanisms*, ed. J. Angeles, Spring-Verlag, 1998.
- [10] E. Shimada, J.A. Thompson, J. Yan, R.J. Wood, and R.S. Fearing, "Prototyping millirobots using dextrous microassembly and folding," *Symp. on Microrobotics ASME Intl. Mechanical Engineering Cong. and Expo.*, Orlando, FL, Nov 2000.
- [11] I. Shimoyama, H. Miura, K. Suzuki, and Y. Ezura, "Insect-like microrobots with external skeletons," *IEEE Control Sys. Magazine*, 13:37–41, February 1993.
- [12] M. Sitti, D. Campolo, J. Yan, R.S. Fearing, T. Su, D. Taylor, and D. Sands "Development of PZT and PZN-PT based unimorph actuators for micromechanical flapping mechanisms," *Int. Conf. on Robotics and Automation*, pages 1509–1516, Seoul, South Korea, 21–26 May 2001.
- [13] R. Wood, R.S. Fearing, "Flight Force Measurements for a Micromechanical Flying Insect," to appear *Int. Conf. Intelligent Robotics and Systems 2001*, Maui, HI, Oct. 29–Nov. 3, 2001
- [14] J. Yan, R.J. Wood, S. Avadhanula, M. Sitti, and R.S. Fearing, "Towards flapping wing control for a micromechanical flying insect," *IEEE Int. Conf. on Robotics and Automation*, pages 3901–3908, Seoul, South Korea, May 2001.
- [15] K. Abe, T. Miwa, and M. Uchiyama, "Development of a 3-axis planar force/torque sensor for very small force/torque measurement," *Trans Jpn Soc Mech Eng*, Vol 42, No. 2, pages 376–382, 1999.
- [16] J. Smits and W. Choi, "The constituent equations of piezoelectric heterogeneous bimorphs," *IEEE Tran. On Ultrasonics, Ferroelectrics, and Freq. Control*, vol. 38, pages 256–270, May 1991.
- [17] M. Weinberg, "Working equations for piezoelectric actuators and sensors," *J. of Microelectromechanical Systems*, vol. 8, pages 529–533, Dec. 1999.